RSC Advances

PAPER

View Article Online
View Journal | View Issue

Cite this: *RSC Adv.*, 2026, **16**, 4157

Nuclear relaxation in agar gel in the presence of highly concentrated PEG coated magnetic nanoparticles at low magnetic fields. Application of temperature dependent T_2^* weighting for MRI thermometry

Janusz H. Hankiewicz, [ab] Giacomo Parigi, [c] Zbigniew J. Celinski,[ad] Yu Hao,[d] Allan D. Angus,[e] Kristen Petersen,[a] Dorota Lachowicz, [f] Angelika Kmita [f] and Marek Przybylski *[fg]

Magnetic nanoparticles are used to map the temperature of the human body using MRI because their presence influences proton relaxation times. Especially at low fields, proton relaxation times exhibit strong temperature dependence, enabling precise determination of local temperature within a body with high resolution. As an illustration, we report temperature-dependent NMR and MRI investigations of agar gel with embedded $Mn_{0.48}Zn_{0.46}Fe_{2.06}O_4$ ferrite nanoparticles, evaluated as potential temperature–sensitive exogenous MRI contrast agents at low magnetic fields for noninvasive MRI thermometry. The nanoparticles consisted of an 8.5 nm magnetic core that were coated with a PEG shell, yielding a hydrodynamic diameter of 20 nm. Spin-lattice relaxation time (T_1) profiles were obtained using a Fast Field Cycling NMR relaxometer. The T_2^* – weighted gradient echo MR images at 0.2 T were obtained in a temperature range of 23 °C to 50.5 °C, encompassing physiologically relevant values. Simulations of MR image intensity at 0.2 T, based on experimental T_1 and T_2^* values, were carried out and compared with the corresponding temperature-dependent experimental images. Analysis of our measurements indicated that the temperature was determined with 2 °C accuracy.

Received 9th October 2025
Accepted 2nd January 2026

DOI: 10.1039/d5ra07731a

rsc.li/rsc-advances

1 Introduction

Reports on nuclear relaxation of water hydrogen protons in aqueous solutions of superparamagnetic nanoparticles indicate that such particles reduce longitudinal relaxation time T_1 at low magnetic fields, with maximum reduction somewhere between 1 MHz and 10 MHz.[1] This observation may allow the use of nanoparticles as contrast agents for T_1 weighted low field MRI as an alternative to agents based on gadolinium chelates.[2] If relaxation times also show strong temperature dependence, magnetic particles can serve functionally as an exogenous temperature contrast agent for MRI thermometry (tMRI). The ability of nanoparticles to influence T_1 in a highly temperature-dependent manner makes them potentially valuable for medical diagnosis, as temperature serves as a crucial indicator of various physiological processes and disease states. Additionally, maintaining precise temperature control during hyperthermia or thermal ablation of cancerous tissues is paramount for ensuring effective treatment while minimizing damage to healthy surrounding tissues.

Recently, we published results on the fabrication technology and comprehensive characterization of polyethylene glycol (PEG) coated mixed copper–zinc (CuZn) and manganese–zinc (MnZn) ferrite nanoparticles. When embedded in tissue mimicking agar gel, CuZn and MnZn ferrite nanoparticles reduce nuclear relaxation times T_1, T_2 and T_2^* of water hydrogen protons at 3.0 T magnetic field. The relaxation times are temperature dependent in the range of 5 °C to 50 °C, giving a necessary temperature contrast for tMRI at 3.0 T.[3,4]

[a]*Center for the BioFrontiers Institute, University of Colorado Colorado Springs, 1420 Austin Bluffs Parkway, Colorado 80918, USA*

[b]*National Institute of Standards and Technology, 325 Broadway St, Boulder, Colorado 80305, USA*

[c]*Department of Chemistry "Ugo Schiff", Magnetic Resonance Center (CERM), University of Florence, Consorzio Interuniversitario Risonanze Magnetiche Metallo Proteine (CIRMMP), Via Sacconi 6, Sesto Fiorentino, 50019, Italy*

[d]*Department of Physics, University of Colorado Colorado Springs, 1420 Austin Bluffs Parkway, Colorado 80918, USA*

[e]*National Society of Professional Engineers-Colorado, PO Box 848, Franktown, CO 80116, USA*

[f]*Academic Centre for Materials and Nanotechnology, AGH University of Krakow, A. Mickiewicza 30, 30-059 Krakow, Poland*

[g]*Faculty of Physics and Applied Computer Science, Academic Centre for Materials and Nanotechnology, AGH University of Krakow, A. Mickiewicza 30, 30-059 Krakow, Poland. E-mail: marprzyb@agh.edu.pl*

MRI thermometry has become a powerful tool in assistance in MRI guided thermal surgeries.[5,6] tMRI delivers real-time 2D temperature maps to assess the progress of thermal treatment of the organ in removing tumours, resection of epileptogenic zones, and correction of vascular malformation, to name a few. Monitoring the temperature simultaneously prevents damage to adjacent tissue and reduces the risk of health-related quality of life outcomes for patients.[7] Details on different tMRI techniques can be found in reviews by Rieke and Odéen.[8,9] Currently, thermally induced water proton resonance frequency (PRF) shift is used to monitor temperature during MRI-guided procedures.[10] In practice, PRF fails due to magnetic field inhomogeneity, tissue movement, or the presence of adipose tissue.[11]

The basic idea behind using magnetic particles as exogenous temperature–sensitive contrast agents for tMRI is to generate temperature-dependent changes in intensity of T_1, T_2 weighted images by spin-echo sequences, or T_2^* weighted images by gradient echo sequences. Then the intensity of these images can be converted into absolute temperature.[12]

In this study, we investigate the nuclear relaxation properties and explore the possibility of using PEG-coated MnZn ferrite nanoparticles in a relatively high concentration as highly specialized temperature–sensitive contrast agents for tMRI at low magnetic fields. We note that MR scanners operating at low magnetic fields usually employ permanent magnets that do not use cryogens. Such magnets are much cheaper to maintain, provide more open space critical for surgical procedures, and can be made mobile.[13,14] These new directions in MRI designs create new opportunities for diagnosing and treatment.

The availability of these low-field MRI systems increases the demand for contrast agents optimized for these lower field strengths. Superparamagnetic nanoparticles are well-suited as positive (T_1 weighted) MRI contrast agents, exhibiting peak relaxation enhancement at around 0.2 T. For instance 8.5 nm commercially available carboxylic acid-coated iron oxide nanoparticles show peak at the body temperature (37 °C) at 0.23 T.[1] The exploitation of ferrite nanoparticles is particularly motivated by the limitations of traditional gadolinium-based agents, which are contraindicated for patients at risk with renal impairment, by the strong temperature dependence of the relaxation enhancement, and because of their possible functionalization with therapeutic agents. Mn-doped ferrite nanoparticles can enhance their magnetic responsiveness and leads to superior magnetic hyperthermia therapy performance, while maintaining small particle size allows renal clearance and good biocompatibility.[15] The development of new contrast agents that allow the performance of MRI-guided thermal ablations using low-field scanners would expand patient treatment options.

The technology we develop, however, is not aiming to replace standard MRI contrast agents delineating different tissues and blood vessels at body temperature (37 °C) such as Gd-based chelates. Unlike standard contrast agents, temperature–sensitive contrast agents do not require high values of relaxivity, but rather its strong temperature changes[16] within the temperature range of interest.

2 Materials and methods

For NMR and MRI experiments, we used PEG-coated MnZn ferrite particles fabricated with a novel one-step technology as described earlier.[4] Here, we briefly summarize the composition and morphology of particles used in this paper and described in detail previously.[4] The final particle composition of $Zn_{0.46}Mn_{0.48}Fe_{2.06}O_4$ was determined using inductively coupled–plasma optical emission spectroscopy. The particle size of 15 nm, including coating, was measured with Atomic Force Microscopy (AFM). The magnetic core size was determined with the transmission electron microscopy to be 8.5 ± 1.0 nm and the hydrodynamic size measured with dynamic light scattering (DLS) was 20 nm.

2.1 Magnetization measurements

The particles' magnetization was studied in a dry form with a superconducting quantum interference device (SQUID) magnetometer (MPMS2 XL with Evercool, Quantum Design, San Diego, CA). The sample was wrapped in 0.06 mm Kapton polyimide film (Cole-Parmer, Vernon Hills, IL, USA) and placed in a straw provided by the manufacturer. The diamagnetic contribution from the straw and Kapton film was not observed. The measurements of magnetization as a function of the magnetic field were performed at 85 K, 315 K and 440 K. Temperature measurements of magnetization were conducted in the temperature range of 5 K to 350 K. The sample was field cooled (FC) at 0.2 T to 4.0 K, and measurements were conducted at constant increments of 5 K.

2.2 Nuclear magnetic T_1 relaxation dispersion profiles

Temperature-dependent longitudinal nuclear magnetic relaxation dispersion profiles (NMRD) of water hydrogen protons were measured in pure agar gel (as diamagnetic reference) and agar gel doped with PEG-coated $Mn_{0.48}Zn_{0.46}Fe_{2.06}O_4$ nanoparticles. Three samples for NMRD were prepared with oxide concentrations of 0.36 mM, 0.73 mM and 1.45 mM in 1% w/w agar gel made with deionized water (DIW). Samples were pipetted to 10 mm diameter, 8-inch-long, flat-bottom NMR glass tubes (type KN8973000008, Millipore Sigma, Burlington, MA).

For the NMRD measurements from 0.2 mT to 990 mT (0.01 MHz to 40 MHz hydrogen proton Larmor frequency), a Fast Field Cycling NMR (FFC NMR) relaxometer was used (Stelar, Spinmaster FFC-2000-1T Mede (PV), Italy) applying the standard FFC NMR technique.[17–19] For the 1.45 mM oxide concentration, NMRD was conducted at temperatures of 10 °C, 20 °C, 30 °C, 40 °C and 50 °C. Measurements of samples with 0.73 mM and 0.36 mM oxide concentrations were conducted only at 20 °C. The error of temperature determination during measurements was ±0.5 °C. The switching time, *i.e.*, the time needed to change the field during cycling, was 3 ms. The T_1 values were obtained with an error smaller than 1% from the fit to a mono-exponential curve of the longitudinal magnetization decay/recovery data acquired at 16 delay times after switching the magnetic field to the desired value.

2.3 Nuclear transverse relaxation time

The temperature dependence of transverse relaxation times T_2 and T_2^* of the sample with 1.45 mM of oxide was measured using a pulse NMR spectrometer operating at 0.36 T, or 15.3 MHz for hydrogen protons, in the range of 5 °C to 50 °C, with 5 °C increments (ElLab, Poznan, Poland). The sample was placed in a standard 5 mm NMR tube (ATS Life Sciences Wilmad, Vineland, NJ)[§§]. The temperature of the sample was controlled by the thermoelectric Peltier device with accuracy of ±0.5 °C.

Spin–spin transverse relaxation time T_2 was measured using the standard CPMG sequence with the following parameters: excitation pulse length $(90^\circ_x) = 2.0$ μs, delay array of 25 delays of 1 ms, generating 25 exponentially decaying spin-echoes after refocusing pulse $(180^\circ_y) = 4.4$ μs, repetition time = 250 ms, number of accumulations = 8.

Values of T_2^* were calculated from the apparent NMR line width $\nu_{1/2}$ (full width at half maximum, FWHM) using the formula:

$$T_2^* = \frac{1}{\pi \upsilon_{1/2}} \quad (1)$$

$\nu_{1/2}$ was obtained from the fitting Fourier Transform of free induction decay (FID) signals to the Lorentzian function. FID signals were acquired after a 2.4 μs RF pulse.[20]

T_2^* measurements by MRI at 0.2 T were conducted using a gradient echo sequence with multiple echo times (TE). An array of 14 TE ranging from 5.75 ms to 35.0 ms was used. To avoid T_1 weighing, the repetition time (TR) was set to 100 ms. Other parameters were: flip angle (FA) = 40°, matrix = 64 × 64 pixels, field of view (FOV) = 30 × 30 mm^2, number of accumulation (NA) = 16, acquisition time for individual TE = 102.4 s, total acquisition time for all 14 TE times = 23 min and 54 s. Because of such a long total acquisition time and constant temperature sweep within the temperature cell, T_2^* measurements by 0.2 T MRI were conducted only at one point when the sample reached the stable thermal equilibrium of 23 °C.

2.4 MRI at 0.2 T

MR temperature-dependent imaging was performed near the minimum of T_1 relaxation time using a 0.2 T scanner (corresponding to 8.5 MHz for hydrogen protons) with a permanent magnet.[21,22] Fig. 1 shows the design of the magnet placed in a temperature-stabilized room at 23 °C to minimize magnetic field temperature drifts. The magnet provides a spherically homogeneous volume for imaging with a diameter of 30 cm (MRI-TECH Canada inc. Cirrus Open MRI). It consists of a top pole (visible in Fig. 1(a)) and a bottom pole (under the scanner cradle, and not visible), which are connected by four columnar ferromagnetic yokes. As mentioned in the introduction, one can appreciate the open-space design of the permanent magnet. The scanner generates a linear magnetic field gradient up to 20 mT m^{-1} in three orthogonal directions within the magnet's homogeneous sphere.

Fig. 1(b), delineated by the dashed green rectangle, shows the RF parallel LC resonator for imaging small objects. This small resonator was used in the study to increase the filling factor and improve the signal-to-noise ratio (SNR). The resonator is made of a standard solenoid and tuning variable capacitor dedicated to nuclei excitement and receiving signals. This is tuned to the ^{1}H resonance frequency of 8.5 MHz. The solenoid consists of 8 loops of 1 mm enamelled copper wire with a length of 15 mm and an inner diameter of 63 mm. The resonator was coupled and matched to 50 Ω transmission/receiving lines using a single coupling loop and a variable capacitor, respectively.

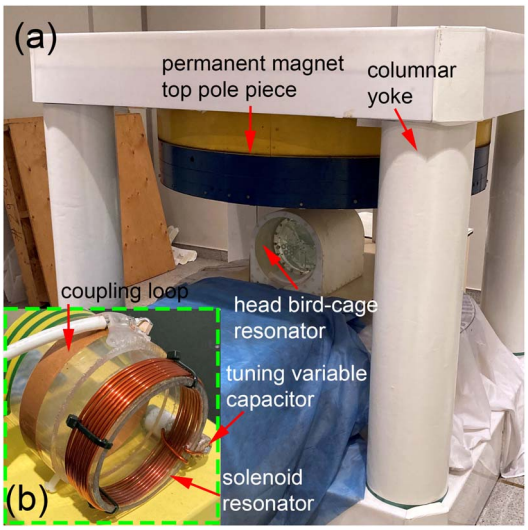

Fig. 1 The design of 0.2 T permanent magnet MRI. (a) General view of the magnet area with the head bird-cage resonator loaded with a spherical head phantom in the imaging position. (b) Photo of the solenoid RF resonator for the imaging of small objects used in this project.

To acquire temperature-dependent images, the phantom was placed in a dedicated MRI-compatible cell. Fig. 2(a) shows a diagram of the cell. The cell comprises a cylinder made of aerogel insulation (Aspen Aerogels, Northborough, MA, USA) and a plastic vial filled with fluorinert (FC-40, 3M Science. Applied to Life, Maplewood, MN). FC-40 is a hydrogen-free electronic liquid that serves as heat energy storage without disturbing MR images. The phantom consists of three glass 10 mm tubes filled with pure agar, agar with 0.73 mM, and an agar with 1.45 mM of oxide. The phantom is inserted in the vial with FC-40. A miniature thermocouple connected to a battery-powered thermometer (Fluke, model 116 HVAC, with a type-K thermocouple, Everett, WA, USA) is immersed in the FC-40 liquid, 40 mm from the MRI axial slice. The tip of the thermocouple is sufficiently far away to avoid potential imaging interference.[23]

Imaging the phantom was conducted during free and uniform cooling from 51 °C to ambient room temperature (23 °C). Individual scans started when the temperature reading reached a whole number, *e.g.* 50 °C, 49 °C, and so on. Because the phantom takes a long time to reach thermal equilibrium (more than 2 hours), there is a gap in MRI temperature measurements at 23 °C and 24 °C points. In the course of cooling, the phantom temperature changed over the duration of

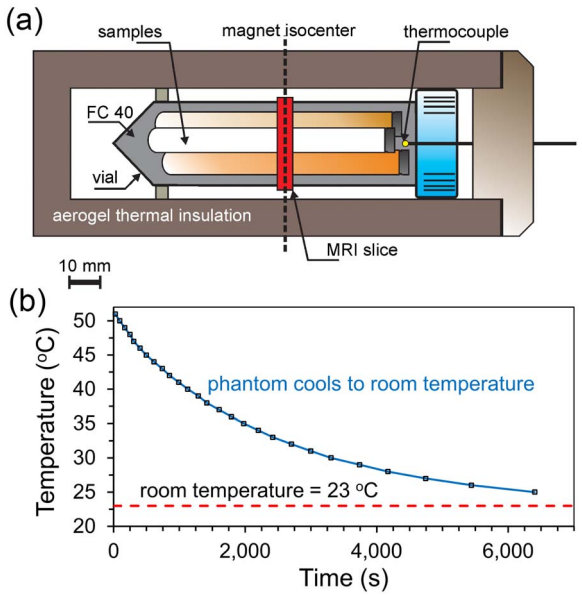

Fig. 2 Temperature dependent MR imaging at 0.2 T. (a) Diagram of MRI compatible cell with the phantom inside. (b) Temperature changes inside phantom as recorded during free cooling (blue solid line) to thermal equilibrium at room temperature (23.0 °C). Black square centres mark consecutive MRI events. Horizontal size of the squares corresponds to 51 s intervals necessary for imaging.

the scan by ±0.4 °C for the first four scans and remained below ±0.3 °C for the other scans.

Gradient echo MR imaging was conducted with the following parameters: TR = 100 ms, TE = 5.75 ms, FA = 40°, FOV = 30 × 30 mm^2, matrix of the axial slice = 64 × 64 (in-plane spatial resolution = 0.47 mm per pixel), slice thickness = 5 mm, number of accumulations = 8, acquisition time = 51 s.

Due to the long minimum available TE = 23.0 ms of the 0.2 T scanner, we were unable to conduct imaging with a standard spin-echo (SE) sequence. Contrary to gradient echo recalled sequence, the spin-echo sequence is known to be more robust and less affected by susceptibility and chemical shift artifacts.[24,25] However, due to a very short relaxation time T_2^* of the agar sample doped with 1.45 mM oxide concentration (less than 8 ms, see discussion in Transverse nuclear relaxation section below), the MR signal after 90° excitation radiofrequency (RF) pulse of the sequence was very low after a 180° RF pulse. Consequently, the signal after image reconstruction within the 1.45 mM oxide sample was not distinguishable from the noise. See an example of the SE image in Appendix A section on Fig. 13.

2.5 Data processing

Raw MRI data from a 0.2 T scanner were reconstructed to images using the internal scanner's software. The binary, spatial domain image files were then converted to a 16-bit tag image file format (TIFF) with an in-house Python-based program. Other experimental data were processed and prepared for this publication using Origin software (Origin-Pro, Version 2023. OriginLab Corporation, Northampton, MA, USA).

3 Results

3.1 Magnetization studies

Our earlier magnetization studies at low magnetic fields show that the magnetic cores of the PEG-coated particles are superparamagnetic, with a blocking temperature around 75 K.[4] Superparamagnetism of particles was confirmed independently by magnetization *versus* magnetic field studies. As shown in Fig. 3(a), the experimental loops do not exhibit hysteresis.[26] We estimated that the magnetization is saturated at approximately 0.5 T field. The temperature dependence of the mass magnetization at a low field of 0.2 T and its comparison to results at a high field of 3.0 T are shown in Fig. 3(b). The solid magenta lines mark the region of temperatures related to the NMR and MRI studies from 278 K to 323 K (5 °C to 50 °C). Although the mass magnetization at 0.2 T is about 15% lower than at 3.0 T, there is a strong and linear temperature dependence of the magnetization both at 0.2 T and 3.0 T. Over the temperature range from 278 K to 350 K, the linear regression analysis returns similar slope values at 0.2 T and 3.0 T of 1.63 × 10^{-2} Am^2 kg^{-1} K^{-1} (R^2 = 0.9998) and 1.68 × 10^{-2} Am^2 kg^{-1} K^{-1} (R^2 = 1.0), respectively. This strong temperature dependence of magnetization is desired for materials destined for tMRI.[27]

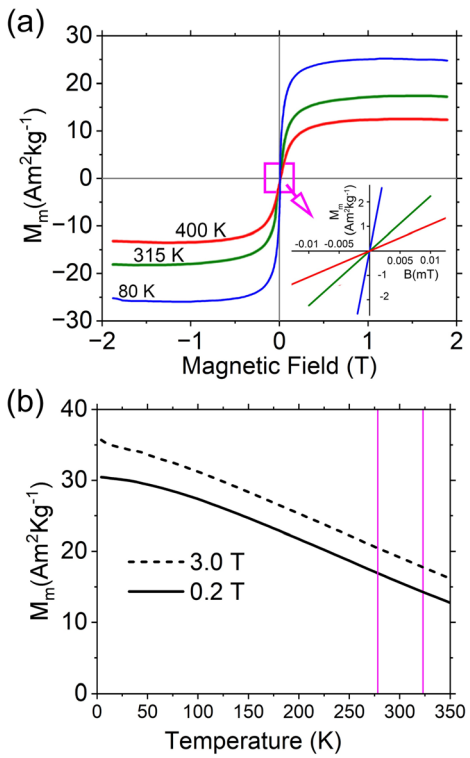

Fig. 3 Magnetization studies of MnZn superparamagnetic nanoparticles. (a) Hysteresis curves at different temperatures show the absence of magnetic remanence and the coercive field. This is particularly visible in an inset (b) Temperature dependence of mass magnetization at 0.2 T and 3.0 T magnetic fields. Vertical solid magenta lines show temperature range of NMR and MRI studies.

3.2 Longitudinal nuclear magnetic relaxation dispersions

Agar gel created using high-purity water exhibits a very long relaxation time T_1 of water hydrogen protons, as shown in Fig. 4(a). This relaxation time remains long even for high agar concentrations, as reported for studies of agar-based tissue-mimicking phantoms.[28] The magnetic field dependence is monotonic and increases to above 4 s at 0.99 T for 50 °C. Adding superparamagnetic particles lowers T_1, which is concentration, temperature and magnetic-field dependent. Fig. 4(b) shows the magnetic field dependence of T_1 of agar gel doped with MnZn ferrite particles at 1.45 mM concentration of oxide for various temperatures. Additionally, the field dependence of T_1, for smaller oxide concentrations of 0.73 mM and 0.36 mM, is shown at 20 °C. Temperature dependence of T_1 in agar gel doped with 1.45 mM concentration of MnZn nanoparticles at 0.2 T is shown on Fig. 4(c).

In the practical application of nanoparticles as temperature–sensitive contrast agents for tMRI, one needs information on the thermal dependence of nuclear relaxation times at a given magnetic field. Fig. 5(a) shows the percentage of T_1 changes relative to the value at 10 °C for selected magnetic fields taken from data presented in Fig. 4(b). The percentage change determines the contrast of T_1 weighted images and directly affects the accuracy of the determination of the temperature. This can be used as an indicator for the optimum magnetic field magnitude. Among the fields collected in the NMRD profiles, the 0.007 T field shows the largest T_1 change, which is shown more clearly in Fig. 5(b) as a local maximum. In this figure, the slope values from Fig. 5(a), normalized to 10–50 °C temperature range, are presented as a function of the magnetic field.

There are only a few MRI scanners available close to 0.1 T, where minimum of T_1 occurs (see Fig. 4(b)), such as the 0.064 T MRI scanner (Hyperfine, Guilford, CT). Our research group had access to a 0.2 T scanner, which operates slightly above the field of a T_1 minimum.

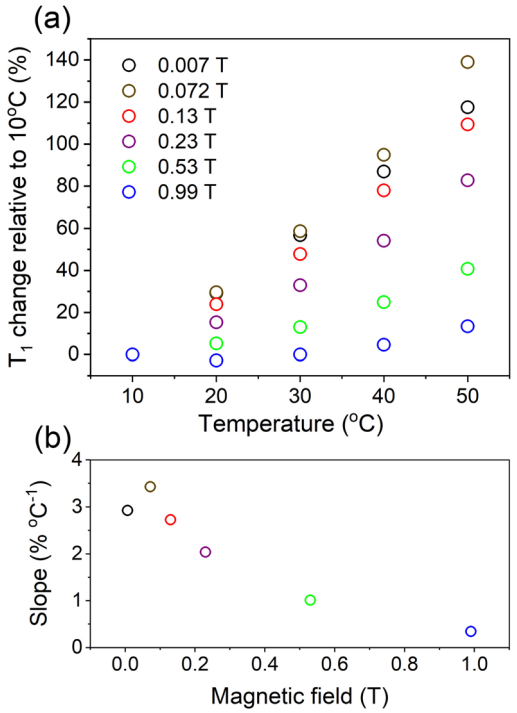

Fig. 5 Temperature and magnetic field dependence of T_1 for water hydrogen protons in agar gel with embedded MnZn iron oxide in concentration of 1.45 mM. (a) Percentage changes of T_1. At various (b) value of the slopes from Fig. 5(a) normalized to 10–50 °C temperature range.

3.3 Dispersions of r_1 relaxivity

For a comparative evaluation of the efficacy of this nanoparticle as an MRI contrast agent and for an analysis with existing models, the relaxivities r_1 of water hydrogen protons in the agar gel samples with embedded nanoparticles of $Mn_{0.48}Zn_{0.46}Fe_{2.06}O_4$ were calculated at various temperatures using the T_1 data presented in Fig. 4(b). The relaxivity r_1 was calculated using the formula:

$$r_1 = \frac{\frac{1}{T_1} - \frac{1}{T_{1\mathrm{dia}}}}{C_{\mathrm{oxide}}} \quad (2)$$

where T_1 is the longitudinal relaxation time of water hydrogen protons in agar gel with embedded particles, $T_{1\mathrm{dia}}$ is the

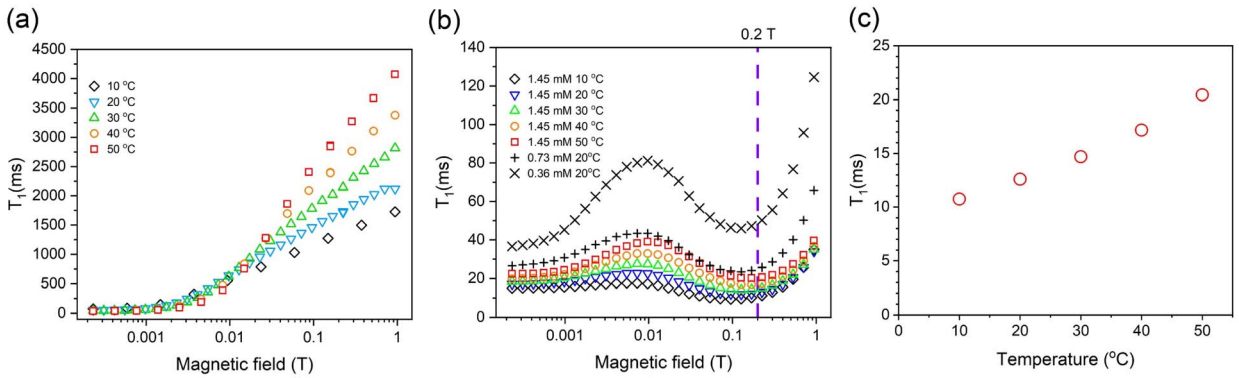

Fig. 4 Water hydrogen protons longitudinal T_1 relaxation dispersions. (a) Field dependence of T_1 in a pure 1% w/w agar gel. (b) Field dependence of T_1 in agar gel doped with MnZn ferrite nanoparticles. Measurements were performed in the range between 0.0002 and 0.99 T at multiple temperatures for the sample with oxide concentration of 1.45 mM, and only at 20 °C for the samples at 0.36 mM (+) and 0.73 mM (x) oxide concentration. Vertical dashed violet line at 0.2 T represents operating frequency of the low-field 8.5 MHz MRI scanner. Note strong reduction of T_1 at 0.2 T. (c) Temperature dependence of T_1 in agar gel doped with 1.45 mM concentration of MnZn nanoparticles at 0.2 T.

longitudinal relaxation time of water hydrogen protons in a pure agar gel, and C_{oxide} is the molar concentration of oxide particles in the agar solution.[29,30] To the best of our knowledge, this study represents the first comprehensive determination of relaxivity for mixed manganese–zinc ferrite nanoparticles across a broad temperature range (from 10 °C to 50 °C) and ^{1}H Larmor frequencies spanning from 0.01 to 40 MHz (see Fig. 6). Observed relaxation rates for 1 mM oxide concentration at the peak position varied from *ca.* 35 s^{-1} (50 °C) to 70 s^{-1} (10 °C). This indicates a relaxivity per 1 mM of paramagnetic metals (iron + manganese) that is 2.54 times smaller. Notably, the relaxivity per 1 mM paramagnetic ion concentration is thus close to, although somewhat smaller than, that reported for non-doped iron-oxide particles of similar size, such as Ferumoxytol, which shows a relaxivity of *ca.* 35 s^{-1} mM^{-1} (of Fe) and 45 s^{-1} mM^{-1} (of Fe) at 37 °C and 22 °C, respectively.[1]

As previously noted,[31,32] the sharp decrease in relaxivity with increasing temperature is primarily ascribed to the increase in the diffusion coefficient: as the temperature rises from 20 °C to 50 °C, the diffusion coefficient almost doubles, and consequently the diffusional time τ_D nearly halves, leading to a corresponding reduction in the relaxation rates at frequencies near the peak position. In lower fields, the temperature dependence is also influenced by the Néel correlation time τ_N, which is likewise expected to decrease as the temperature increases.

For all temperatures, the relaxivity profiles shown in Fig. 10 exhibit three common features: (1) a low-field plateau, (2) a maximum around 0.15 T, and (3) a rapid decrease above 0.15 T. At very low magnetic fields, the fluctuating part of the magnetic moment of the superparamagnetic particle, μ_{NP}, aligns along an easy magnetization direction and randomly jumps from one easy direction to another with a characteristic time called Néel correlation time.[33] As the applied magnetic field increases, the non-zero time average part of μ_{NP}, called the Curie-spin magnetic moment, aligns with the direction of the magnetic field and increases up to saturation. The observed maximum of r_1 around 6 MHz (0.15 T) originates from two mechanisms: the gradual increase of the Curie-spin magnetic moment with the applied magnetic field and the subsequent decrease of the spectral density function at frequencies on the order of, or larger than, the inverse of the translational diffusion correlation time (τ_D). As the magnetic field increases, the relaxivity decreases.[34–36]

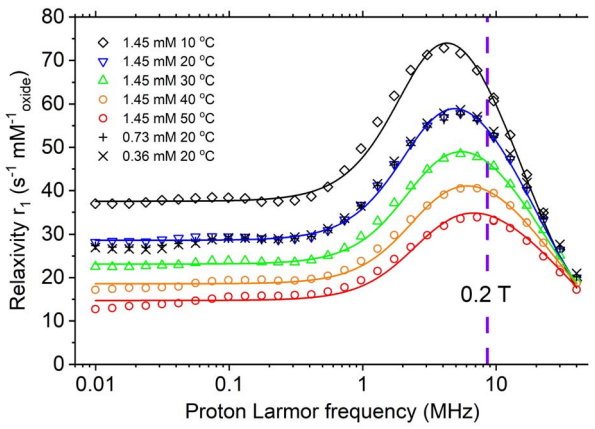

Fig. 6 Relaxivity profiles r_1 for water hydrogen protons in the agar gel with embedded nanoparticles of $Mn_{0.48}Zn_{0.46}Fe_{2.06}O_4$ ferrite in 1.45 mM concentration of oxide, at various temperatures. Markers + and x indicate data at 20 °C for concentrations of 0.73 mM and 0.36 mM, respectively. Solid lines represent the fit to the Roch–Müller–Gillis model (see for details in Appendix C). Violet dashed vertical line shows 8.5 MHz operating frequency of the MRI scanner used for temperature dependent imaging (Larmor frequency for hydrogen protons at 0.2 T).

3.4 Transverse nuclear relaxation

As stated in the Materials and methods section above, due to the long acquisition time of the T_2^* mapping MRI sequence and simultaneous temperature change within the phantom holding cell, T_2^* measurements at 0.2 T were conducted only at 23 °C, when the sample reached thermal equilibrium with the magnet room. The temperature dependence of T_2^* was thus observed at 0.36 T, as a guide for planning of T_2^* weighted gradient echo MRI protocols, and for the image intensity simulations. Fig. 7 shows the transverse relaxation time T_2^* measured at 0.36 T in the range between 5 °C to 50 °C and the value measured at 0.2 T and 23 °C. Additionally, the figure also presents the temperature dependence of the T_2 relaxation, as useful information for possible spin-echo imaging. One can appreciate that the 23 °C value of T_2^* for the concentration of 1.45 mM at 0.2 T fits nicely into the 0.36 T temperature data trend, justifying the use of T_2^* measured at 0.36 T data for the following 0.2 T MRI experiments and signal simulation, as shown in the subsequent section.

3.5 MRI at 0.2 T

The 0.2 T low field scanner has hardware-imposed limits on the minimum available echo time (TE_{min} = 5.75 ms) in gradient echo sequence. With such relatively long TE, and short T_2^* of samples in the phantom, the images were inherently T_2^*

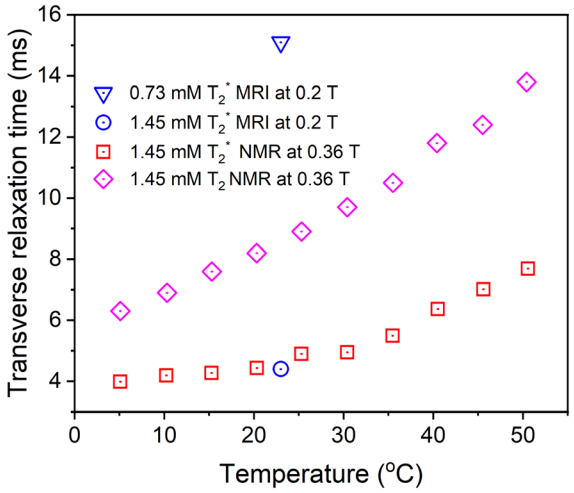

Fig. 7 Temperature dependence of the transverse relaxation times T_2 and T_2^* of water hydrogen proton in the presence of 1.45 mM concentration of MnZn iron oxide at 0.36 T. Additional values of T_2^* are shown from 0.2 T MRI at 23 °C for 0.73 mM and 1.45 mM oxide.

weighted and, as a result, T_1 weighted temperature-dependent studies at 0.2 T were not possible. Therefore, we focused on testing whether T_2^* weighted images provide temperature-dependent contrast useful for tMRI. We benefited from the very short T_1 in another way, as it enabled fast scanning with multiple accumulations, leading to an improved SNR and better temporal resolution of the method.

Fig. 8 shows representative gradient recalled echo images at three selected temperatures. Images are T_1 weighed for pure agar gel. Images of MnZn iron oxide solutions in agar are T_2^* weighted (T_1 is shorter than 20 ms and T_2^* increases from 4.0 ms to 7.7 ms in the temperature range from 23 °C to 50.5 °C) and their brightness increases with temperature.

The image intensity was analyzed within a selected circular region of interest (ROI) consisting of 274 pixels. Details of this analysis are presented in Fig. 9. Fig. 9(a) shows the thermal dependence of the mean value of the image intensity. The inset in the bottom-right corner shows the positions of four ROIs corresponding to pure agar, 0.73 mM and 1.45 mM oxide concentration in agar, and the background noise.

By assumption, the measured noise shown in Fig. 9(b) originates from Johnson–Nyquist thermal noise in both the real and imaginary parts of the complex MRI signal. This noise is squared and summed, at which point the distribution is χ^2 of order two, since two Gaussian distributions have been squared and added together. Once one takes the square root of this noise, one obtains a Rayleigh distribution for the noise in a non-signal part of the image.

From Cárdenas-Blanco,[37] eqn (17), we have $m_R = \sigma_g\sqrt{\frac{\pi}{2}} \approx 1.253\cdot\sigma_G$ where m_R is our measured noise in the Fig. 9(b) and σ_G is the standard deviation of the desired input-referred Gaussian noise. We find that the measured variation in this noise is somewhat larger across the 25 °C temperature range of the experiment, assuming the expected values from $\sqrt{4\cdot k_B\cdot R\cdot B_w\cdot T}$, where k_B is Boltzmann's constant, R is the effective resistance, B_w is the bandwidth, and T is the temperature in Kelvin. Our working hypothesis is that this extra variation arises from a thermal detuning of the parallel resonant circuit shown in Fig. 1(b), with the center frequency shifting away from the desired signal frequency.

Fig. 9(b) also shows a linear regression fit of experimental noise with Pearson's $r = 0.7784$ and $R^2 = 0.6059$ (solid black line) and estimated values of σ_G (solid red line). Using these estimates of σ_G, we computed measured average values M_{AVE} of the vial signals in SNR form as M_{AVE}/σ_G. While these SNR values were greater than 5, we proceeded to calculate actual signal-to-noise values, A/σ_g using Henkelman.[38] $A/\sigma_G = \sqrt{(M_{AVE}/\sigma_G)^2 - 1}$ These final SNR values are shown in Fig. 9(c).

Fig. 9(d) presents the results of our major objective: the thermal dependence of the SNR of water hydrogen protons T_2^* weighted images due to the presence of ferromagnetic particles. The figure includes a linear fit to experimental points as well as 95% prediction bands. The prediction bands were used for the determination of accuracy of the method at 38 °C, the temperature slightly above the human body physiologically relevant temperature of 37 °C.[39] The accuracy Δt at given temperature t in degrees Celsius is defined by the range, within which the temperature determination from MR image intensity is statistically not distinguished from temperatures below (−) and above (+) using 95% prediction bands. Details of the accuracy analysis are presented in Appendix B, and the analysis results are shown in Table 1.

As shown in Table 1, the slope values directly relate to the accuracy of temperature determination. For the two concentrations studied here, the steeper slope corresponding to 1.45 mM concentration gives better accuracy. Poor accuracy of −7.5 °C/+6.4 °C renders the 0.73 mM concentration too small for practical use. Doubling the concentration to 1.45 mM delivers a much better accuracy (−2.2 °C/+2.3 °C).

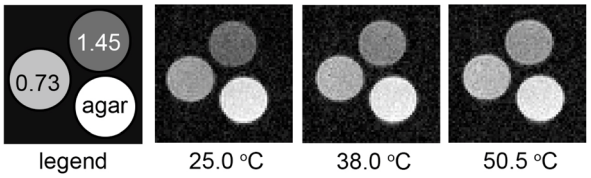

Fig. 8 Representative gradient echo MR axial images acquired at select temperatures of the phantom at 0.2 T. The description of the phantom is shown in the legend panel on the left. Agar denotes pure 1.0% w/w of agar solution in DIW, numbers 0.73 and 1.45 are MnZn iron oxide concentration in agar gel in mM. Images were acquired during cooling (from 50.5 °C to 25 °C, corresponding to the temperature registered at the beginning of each scan) of the phantom.

4 Discussion

4.1 Profiles of r_1 relaxivity

The nuclear relaxation of water in agar gel samples with embedded nanoparticles is caused by modulations of the dipole–dipole interaction between the magnetic moment of water hydrogen protons and the magnetic moment of superparamagnetic particles μ_{NP}.[40] The dynamic process modulating this dipolar interaction is the translational diffusion of water hydrogen protons as shown graphically in Fig. 10. Large nanoparticles of the MnZn ferrite are trapped in complex repeated units of polysaccharide that form agar gel.[41] Despite being relatively stiff, the 1% agar gel samples allow small water molecules to move freely. The interactions between water hydrogen proton spin magnetic moments and the nanoparticle's magnetic moment μ_{NP} thus fluctuate with a correlation time τ_D that depends on the distance of the closest approach (d) between water hydrogen proton spins and the nanoparticle magnetic moment. It also depends on the diffusion coefficient of water molecules (D).

$$\tau_D = \frac{d^2}{D} \quad (3)$$

For PEG coated nanoparticles, the presence of the shell increases the distance of the closest approach, as shown in Fig. 9.

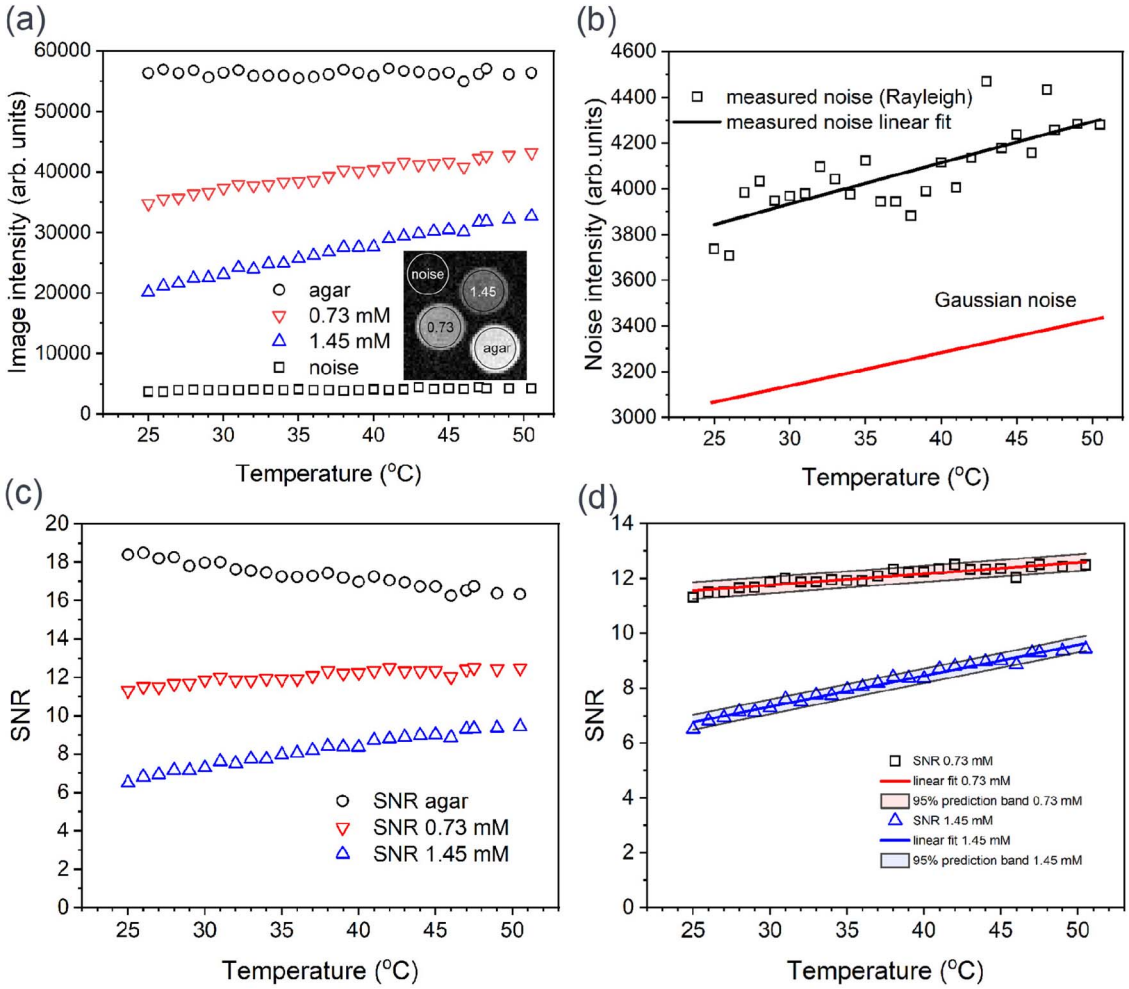

Fig. 9 Analysis of phantom temperature dependent noise and images intensity. (a) Experimental image intensity (M_{AVE}) obtained from 274-pixel region of interest (ROI) in circles shown in the inset on right bottom. (b) Noise intensity. Black squares is a background Rayleigh noise measured at ROI shown in (a), black solid line is a linear fit to the Rayleigh experimental noise. Red line is derived from Rayleigh noise fit to estimate input Gaussian noise for calculations of SNR. See text for details. (c) Estimated SNR. (d) Statistical analysis of image SNR of ROI within 0.73 mM and 1.45 mM phantom. Markers represent calculated data points, red and blue solid lines are corresponding linear fits, and black solid lines delineate the 95% prediction band areas.

Table 1 Slopes of linear fits shown in Fig. 8(d) and the accuracy of the temperature determination using MR signal intensity from T_2^* weighted images, of samples with 0.73 mM and 1.45 mM concentration of MnZn iron oxide in 1% (w/w) agar gel

Concentration (mM)	Slope (°C^{-1})	Accuracy (°C)
0.73	0.041	−7.2/+7.6
1.45	0.113	±2.2

The experimental r_1 profiles were fit to the Roch–Müller–Gillis model with d and single large spin (S) resulting from the coupling of all electron spins in each nanoparticle as common parameters.[42] Solid lines in Fig. 6 represent the best fit with parameters shown in Table 2. Details of the model are provided in the Appendix C section. Water diffusion at 20 °C and 50 °C used for the best fit was fixed to the experimental results reported earlier.[4] The best-fit value of the distance of closest approach equals 7.0 nm and is intermediate between the value of 4.75 nm of the magnetic core and 7.5 nm of the shell experimentally determined by AFM. Néel correlation times of a few nanoseconds and an S value approaching 10 000 are obtained similarly to other iron oxide nanoparticles of similar size.[1,43] The good quality of the fit across all profiles acquired in this wide temperature range also validates the Roch–Müller–Gillis theory for manganese-doped ferrite nanoparticles.

4.2 Thermal MRI contrast

The MRI contrast at 0.2 T obtained from T_2^* weighted experimental data was analyzed against T_2^* weighted MRI signal intensity simulations. For comparison purpose we calculated the MRI signal using eqn (4).[44] As explained in Material and method section, due to limitations of the MRI scanner, we were unable to obtain experimental data for T_1 weighting.

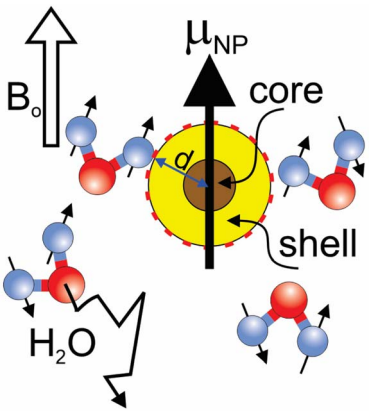

Fig. 10 Illustration of the dipole–dipole interaction between the magnetic moments of hydrogen protons of freely diffusing water molecules (black solid arrows) and stationary nanoparticle magnetic moment (μ_{NP}) in the presence of the static magnetic field B_o. Note the shell around the core increases the distance of the closest approach (d) to 7.5 nm, as calculated from AFM.

Table 2 Temperature dependent parameters for best fit of relaxivity r_1 data presented in Fig. 10: water diffusion (D), Néel correlation time τ_N, distance of the closest approach (d), single large spin resulting from the coupling of all electron spins in each nanoparticle (S), and concentration (C). In parentheses are experimental results: *published earlier[4] and #from this paper. The symbol & indicates that the value was fixed in the fit analysis

t (°C)	10	20	30	40	50
D (10^{-9} m^2 s^{-1})	1.43	1.97*&	2.52	3.16	3.86*&
τ_N (10^{-9} s)	4.54	3.54	2.92	2.35	1.83
d (nm)					7.0 (7.5)#
S					8900
C (mM)					1.45#&

$$SI = k[H]\frac{\sin(FA)\left(1 - e^{-\frac{TR}{T_1}}\right)}{(1 - (\cos(FA)))e^{-\frac{TR}{T_1}}}e^{-\frac{TE}{T_2^*}} \quad (4)$$

where: $k[H]$ is the Boltzmann weighting factor $\left(k[H] = \frac{2\mu_B H}{k_B T}\right)$; μ_B is Bohr's magneton for protons, k_B is the Boltzmann constant, T is temperature. For the studied temperature range of 23 °C to 50.5 °C and a magnetic field of 0.2 T, a weighting factor $k[H] \cong 1$ is obtained. FA is the flip angle (rad), TR is repetition time, and TE is echo time; these are MRI sequence parameters set by an operator using guidance from relaxation measurements.

Experimental relaxation values of T_1 and T_2^*, and values of the TR, TE and FA parameters used in the MRI sequence to achieve the T_2^* weighting contrast are given in Table 3. Note that values of T_1 are from 0.2 T NMRD, while values of T_2^* are obtained from 0.36 T NMR studies. Results for TR/TE = 35.0/5.75 ms are slightly T_1 weighted at higher temperature when T_1 reaches a value of 20.4 ms.

Results of the simulations, and experimental T_2^* weighted MRI, are shown in Fig. 11(a). The intensities of T_2^* weighted images obtained from the simulation and from the experiments are increasing with temperature as the particles' magnetization decreases (see Fig. 3) and are in good agreement with each other. The paired t-test shows that at the level of 0.05, the difference between signal intensity for experimental T_2^* weighting and simulated T_2^* weighting is not significant.

The values of simulated signal intensities (SI) presented in Fig. 11(a) were used for the calculations of temperature MRI contrast between 30 °C and 50 °C using eqn (5).[45]

$$\text{Temperature contrast} = SI_{30\ ^\circ Co} - SI_{50\ ^\circ Co} \quad (5)$$

The results of contrast values for T_2^* weighted experiments and T_2^* weighted simulations are in good agreement, −0.09 and −0.10, respectively (see Fig. 11(b)).

Since the acquisition time of the current T_2^* weighted image is relatively long, we simulated the possible shortening of TR to achieve better temporal resolution of the temperature determination. Shortening TR from 100 ms to 35 ms lowers the MRI signal by only 1% and sacrifices the contrast by 10%, while simultaneously decreasing the image acquisition time from 6.4 s to 2.2 s. Shortening acquisition time is critical because during MRI-guided procedures, temperature information must be obtained in real time.

4.3 Method limitations and clinical relevance

The safety of *in vivo* use of MnZn nanoparticles is presently unknown. However, the growing interest in the use of iron-oxide base nanoparticles as MRI contrast agents stimulates research on toxicity and such materials. For instance, the modified magnetite nanoparticles available in the form of iron supplements such as Feraheme are currently accepted for intravenous infusion by FDA and are evaluated for use in magnetic fluid hyperthermia[46] and as MRI vascular contrast agents at low-field MRI scanners.[47]

The proposed method of temperature measurement intrinsically suffers from the dependence of MRI temperature contrast on magnetic particle concentration. This issue can be partially alleviated by using thin filaments made of hydrogen-rich polymers with embedded particles. Although more invasive, the method can provide an MRI-compatible means of measuring temperature in one direction by thermal contact between a filament and the tissue.

As mentioned in the Introduction, PRF fails in areas rich with adipose tissue due to the complexity of the proton NMR line[48] and the small temperature-dependent chemical shift.[49,50] There is growing evidence that patients with obesity are at high risk of developing tumours[51] and will potentially require surgery using MRI-guided thermal ablations in areas of high fat content.[52] As temperature monitoring by PRF in such cases will not be reliable, we envision injections of temperature sensitive particles in fat tissue at the surgery location. Then T_2^* maps will be acquired of the region of injection and compared to the

Table 3 NA stands for not available data of T_2^* at 0.2 T. Parameters used for weighted MRI signal intensity experiment and simulations. Experimental values of T_1 and T_2^* used are presented in Fig. 4c and 6, respectively

		T_1 (ms) at		T_2^* (ms) at				
	Weighting by	30 °C	50 °C	30 °C	50 °C	TR (ms)	TE (ms)	FA (°)
Experiment	T_2^*	14.7	20.4	NA	NA	100	5.75	40
Simulation	T_2^*	14.7	20.4	4.95	7.69	100	5.75	40
Simulation	T_2^*	14.7	20.4	4.95	7.69	100	2.0	40
Simulation	T_2^*/T_1	14.7	20.4	4.95	7.69	35	5.75	40

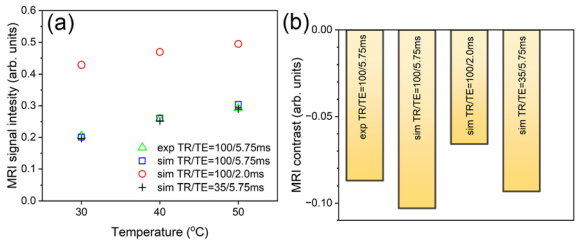

Fig. 11 Experimental data (exp) and numerical simulations (sim) using NMR relaxation data for 1.45 mM concentration at 0.2 T. (a) MRI signal intensity for simulated T_2^* weighting conditions and comparison with experimental T_2^* weighting experimental results. For comparison purposes, the signal's experimental intensity was normalized to match the simulated intensity at 30 °C. (b) MRI contrast calculated from results in (a). See the text for details.

temperature calibration map obtained earlier from fatty phantom with particles injected in the same amount to convert T_2^* maps to temperature maps as temperature changes.

5 Conclusions

MnZn ferrite nanoparticles embedded in agar gel at 1.45 mM oxide concentration can deliver T_2^* MRI temperature contrast, permitting non-invasive temperature measurements. Signal intensity of T_2^* weighted images obtained with the standard gradient echo sequence at 0.2 T near the physiological temperature of the human body (38 °C) delivers the accuracy of temperature determination of ±2.2 °C. Since the T_1 time of free water protons in the agar phantom doped with nanoparticles is very short, image acquisition can be performed in 6.4 s. A shorter acquisition time, leading to better temporal resolution for the method, is possible by reducing TR, with some sacrifice in SNR and contrast.

As seen in Fig. 8, due to the long minimum TE time (5.75 ms), the standard gradient echo recalled sequence available on a 0.2 T scanner, delivers images from an aqueous phantom with embedded high concentration of MnZn nanoparticles with relatively low value of SNR. Use of high-end gradient equipment with much shorter TE = 2.0 ms as shown with the simulation will slightly improve SNR. Imaging the tissue with high concentrations of magnetic nanoparticles would benefit from much higher SNR achieved with the newly developed sequences with minimal TE such as Ultrashort Echo Time (UTE) or Zero Echo Time (ZTE).[53] Theoretical analysis shows new ways of achieving selective T_2 contrast using UTE sequence.[54] Positive T_1 weighted contrast obtained experimentally with UTE was reported in tissues with targeted iron-oxide nanoparticles at 3.0 T magnetic field.[55] T_2^* relaxometry in the presence of highly concentrated iron-oxide nanoparticles (close to concentrations presented in this paper) labelled cels at 3.0 T using 3D UTE was also published.[56] Its prohibitively long acquisition time of 39 minutes can be shorten by reducing acquisition space to 2D. However, the practical exploit of our observation on the maximum of the water proton r_1 relaxivity near 0.15 T in a phantom with high concentration of MnZn magnetic particles, and to use it for the temperature mapping in low-field scanners is currently limited due to the absence of the implementation of very short echo-time sequences at low fields.

Author contributions

Janusz H. Hankiewicz: conceptualization, methodology, investigation, formal analysis, writing original draft, review and editing, data curation. Giacomo Parigi: investigation, formal analysis, review and editing. Zbigniew J. Celinski: conceptualization, review and editing. Yu Hao: software. Allan D. Angus: MR images noise analysis, Kristen Petersen: writing original draft, review and editing. Dorota Lachowicz: investigation. Angelika Kmita: investigation. Marek Przybylski: funding acquisition, supervising, review and editing.

Conflicts of interest

There are no conflicts to declare.

Data availability

Data for this article, including SQUID, low field NMR, NMRD and MRI are available at database Figshare.com at URL https://doi.org/10.6084/m9.figshare.29967883.

A Appendices

A.1 Spin-echo imaging at 0.2 T

As mentioned in the Material and method section above, we attempted to conduct the spin-echo imaging at 0.2 T. Fig. 12 below illustrates a preliminary scout image taken at 23 °C of the phantom that contains pure agar gel and agar gel with 0.73 mM and 1.45 Mm concentration of MnZn iron oxide. Imaging

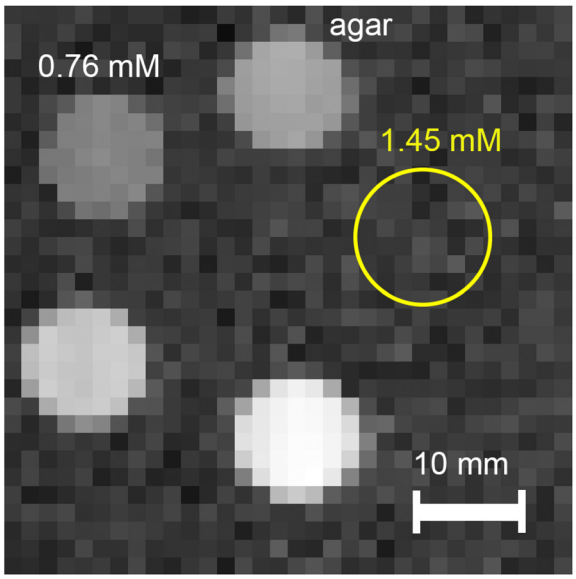

Fig. 12 MR imaging in the field of 0.2 T and at 23 °C using the spin-echo sequence. Yellow circle marks area of the location of 1.45 mM concentration sample. Due to short T_2 and long TE, signal from water hydrogen proton in this area is not visible. Longer T_2 of concentration 0.73 mM, allows the sample visualization.

parameters were as follows: TR = 500 ms, TE = 23.0 ms, FOV = 50 × 50 mm^2, slice thickness = 5 mm, matrix = 32 × 32. With an inherently long echo time of the scanner of 23.0 ms combined with a short relaxation time T_2 of 1.45 mM concentration (8.5 ms) the part of the image that covers this concentration is heavily T_2 weighted and is not visible. In Fig. 12, the cross-section of the 1.45 mM sample should appear in the area marked by a yellow circle. As seen in the top left corner of Fig. 12, the longer T_2 time of 0.73 mM concentration allows for the visualization of this part.

A.2 Accuracy of temperature determination

The accuracy of non-invasive determination of the temperature by using the temperature sensitive MRI contrast agent was calculated from images obtained with 0.2 T scanner at 38 °C (close to the physiological temperature of humans) using 95% prediction bands obtained from statistical analysis of image intensity within image ROI containing 274 pixels of 0.73 mM and 1.45 mM samples (see Fig. 13). The intersections of the horizontal dashed lines that cross the 95% prediction bands limit (solid black lines) at 38 °C were projected on the horizontal temperature axis (along dash-dot red lines), giving the boundaries of the temperature determination error.

A.3 Fitting the r_1 relaxivity profiles

The relaxivity r_1 profiles shown in Fig. 10 were obtained using relaxation rates R_1^{out} calculated from eqn (A1)fd2 below.[35]

In the fit analysis the following parameters were optimized: the distance of the closest approach, d, the single large spin (superspin) in each nanoparticle, S, resulting from the coupling

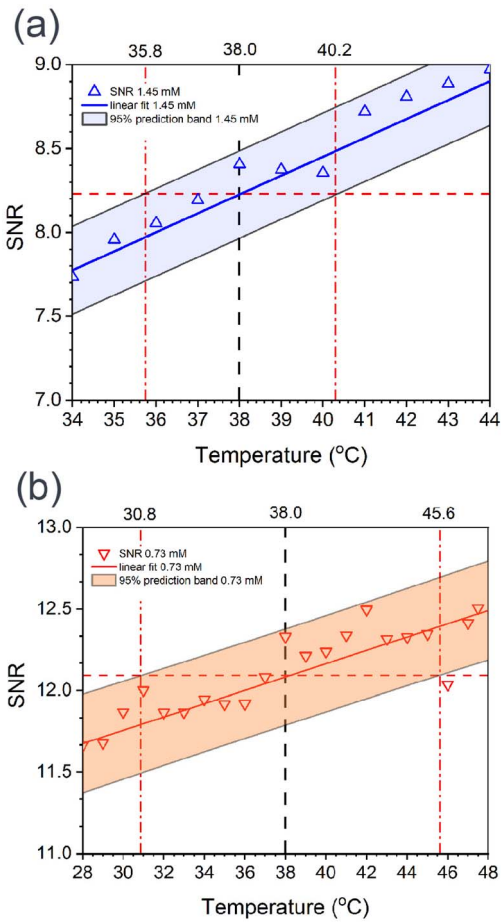

Fig. 13 Determination of the accuracy of the method at 38 °C. (a) Area of 95% prediction band for 1.45 mM is marked by blue color. Accuracy is ±2.2 °C. (b) Area of 95% prediction band for 0.73 mM is marked by orange color. Accuracy is −7.2 °C/+7.6 °C.

of all electron spins in a nanoparticle, the diffusion coefficient, D, and the Néel correlation time, τ_e.

The other parameters entering the above equation are the Avogadro's constant N_A, the molar concentration of the nanoparticles M (in mol L^{-1}), the proton gyromagnetic ratio, γ_I, the proton Larmor angular frequency ω_I, the Bohr magnetron μ_B, the electron's g-factor g_e, the Langevin function $L(x) = \coth x - \frac{1}{x}$, where $x = \frac{S\hbar\omega_S}{k_B T}$, the electron Larmor frequency $\omega_S = \frac{\mu_B g_e B_o}{\hbar}$, the translational diffusion time $\tau_D = \frac{d^2}{D}$, the heuristic parameters P and Q, and the spectral density functions $J^A(\omega_I, \tau_D)$ and $J^F(\omega_I, \tau_D, \tau_e)$,

$$R_1^{out} = \frac{32\pi}{135}\left(\frac{\mu_0}{4\pi}\right)^2 \frac{1000 N_A M (\gamma_I \mu_B g_e)^2 S^2}{dD}\left\{3[L(x)]^2 J^A(\omega_I, \tau_D) + \left[3\left(1 - 2\frac{L(x)}{x} - [L(x)]^2\right) + 7Q\frac{L(x)}{x}\right] J^F(\omega_I, \tau_D, \tau_e) + 7P\frac{L(x)}{x} J^F(\omega_0, \tau_D, \tau_e)\right\} \quad \text{(A1)}$$

The P and Q parameters account for anisotropic effects at low fields, and when the anisotropic energy is much larger than the Zeeman energy, for frequencies smaller than τ_c^{-1}, the values of P and Q are equal to 0 and 1, respectively. In such cases, the quantization axis of the electron magnetic moment is fixed along the easy axis of magnetization. In our analysis we set $P = 0$ and $Q = 1$.

The spectral density functions are

$$J^{A}(\omega, \tau_D) = \frac{1 + \frac{5z}{8} + \frac{z^2}{8}}{1 + z + \frac{z^2}{2} + \frac{z^3}{6} + \frac{4z^4}{81} + \frac{z^5}{81} + \frac{z^6}{648}} \quad \text{(A2)}$$

where $z = (2\omega\tau_D)^{1/2}$, and

$$J^{F}(\omega, \tau_D, \tau_e) = \mathrm{Re}\left[\frac{1 + \frac{\Omega}{4}}{1 + \Omega^{1/2} + \frac{4\Omega}{9} + \frac{\Omega^{3/2}}{9}}\right] \quad \text{(A3)}$$

where $\Omega = i\omega\tau_D + \tau_D/\tau_e$.

Acknowledgements

Authors thank Dr Krzysztof Klodowski from the University of Cambridge, U.K. for assistance in conducting 0.2 T MRI experiments at AGH University of Krakow, Poland. We acknowledge the help of Mr John Stroud from the University of Washington in Seatle in 0.36 T NMR measurements. We thank Dr Sam Oberdick from NIST in Boulder, CO and Dr Natalia Babayevska from A. Mickiewicz University in Poznan, Poland for the discussion. This study was supported in part by a gift from the Kairos Ventures to UCCS BioFrontiers and by the program "Excellence initiative research university" for the AGH University of Krakow. The authors acknowledge the support and the use of resources of Instruct-ERIC, a landmark ESFRI project, and specifically the CERM/CIRMMP Italy center.

References

1 S. D. Oberdick, K. V. Jordanova, J. T. Lundstrom, G. Parigi, M. E. Poorman, G. Zabow and K. E. Keenan, *Sci. Rep.*, 2023, **13**, 11520.
2 A. Avasthi, C. Caro, E. Pozo-Torres, M. P. Leal and M. L. García-Martín, *Top. Curr. Chem.*, 2020, **378**, 40.
3 D. Lachowicz, J. Stroud, J. H. Hankiewicz, R. Gassen, A. Kmita, J. Stepień, Z. Celinski, M. Sikora, J. Zukrowski, M. Gajewska and M. Przybylski, *Chem. Mater.*, 2022, **34**, 4001–4018.
4 D. Lachowicz, A. Kmita, M. Gajewska, E. Trynkiewicz, M. Przybylski, S. E. Russek, K. F. Stupic, D. A. Woodrum, K. R. Gorny, Z. J. Celinski and J. H. Hankiewicz, *IJMS*, 2023, **24**, 16458.
5 W. M. W. Gedroyc, *Top. Magn. Reson. Imag.*, 2005, **16**, 339–353.
6 N. J. McDannold and F. A. Jolesz, *Top. Magn. Reson. Imag.*, 2000, **11**, 191–202.
7 D. A. Woodrum, S. Zawada and L. A. Mynderse, *Medical Research Archives*, 2024, **12**(9), DOI: 10.18103/mra.v12i9.5779.
8 V. Rieke and K. Butts Pauly, *Magn. Reson. Imaging*, 2008, **27**, 376–390.
9 H. Odéen and D. L. Parker, *Prog. Nucl. Magn. Reson. Spectrosc.*, 2019, **110**, 34–61.
10 J. Blackwell, M. J. Kraśny, A. O'Brien, K. Ashkan, J. Galligan, M. Destrade and N. Colgan, *Magn. Reson. Imaging*, 2022, **55**, 389–403.
11 P. Wang, *Quant. Imaging Med. Surg.*, 2017, **7**, 259–266.
12 J. H. Hankiewicz, Z. Celinski, K. F. Stupic, N. R. Anderson and R. E. Camley, *Nat. Commun.*, 2016, **7**, 12415.
13 T.-O. Liang, Y. H. Koh, T. Qiu, E. Li, W. Yu and S. Y. Huang, *J. Magn. Reson.*, 2022, **345**, 107309.
14 S. Huang, Z. H. Ren, S. Obruchkov, Ji. Gong, R. Dykstra and W. Yu, *Investig. Magn. Reson. Imaging*, 2019, **23**, 179.
15 J. Y. Lee, Y. R. Na, C. M. Na, P. W. Im, H. W. Park, M. K. Kim, Y. Kim, J. H. You, D. S. Kang, H. E. Moon, H. R. Park, M. G. Kim, P. Kim, S. H. Park, H. W. Youn, Y. D. Son, Y. Takemura, C. W. Song, D. Ling, Y. Piao and S. H. Paek, *Theranostics*, 2025, **15**, 2883–2902.
16 J. Stroud, Y. Hao, T. S. Read, J. H. Hankiewicz, P. Bilski, K. Klodowski, J. M. Brown, K. Rogers, J. Stoll, R. E. Camley, Z. Celinski and M. Przybylski, *Magn. Reson. Imaging*, 2023, **100**, 43–54.
17 I. Bertini, C. Luchinat, G. Parigi and E. Ravera, *NMR of Paramagnetic Molecules: Applications to Metallobiomolecules and Models*, Elsevier, Amsterdam, 2nd edn, 2017.
18 C. Luchinat and G. Parigi, *J. Am. Chem. Soc.*, 2007, **129**, 1055–1064.
19 A. T. Preslar, G. Parigi, M. T. McClendon, S. S. Sefick, T. J. Moyer, C. R. Haney, E. A. Waters, K. W. MacRenaris, C. Luchinat, S. I. Stupp and T. J. Meade, *ACS Nano*, 2014, **8**, 7325–7332.
20 T. C. Farrar and E. D. Becker, *Pulse and Fourier Transform NMR: Introduction to Theory and Methods*, Academic Press, Orlando San Diego New York, 1971.
21 K. Kłodowski, J. Kamiński, K. Nowicka, J. Tarasiuk, S. Wroński, M. Świętek, M. Błażewicz, H. Figiel, K. Turek and T. Szponder, *Computerized Medical Imaging and Graphics*, 2014, vol. 38, pp. 458–468.
22 M. Suchanek, M. Kordulska, Z. Olejniczak, H. Figiel and K. Turek, *Postharvest Biol. Technol.*, 2017, **124**, 100–106.
23 W. E. Kwok, *JCIS*, 2024, **14**, 33.
24 B. A. Jung and M. Weigel, *Magn. Reson. Imaging*, 2013, **37**, 805–817.
25 M. Markl and J. Leupold, *Magn. Reson. Imaging*, 2012, **35**, 1274–1289.
26 H. Mamiya and B. Jeyadevan, *IEEE Trans. Magn.*, 2014, **50**, 1–4.
27 J. Stroud, J. H. Hankiewicz, R. E. Camley and Z. Celinski, *J. Magn. Reson.*, 2021, **333**, 107108.
28 A. Antoniou, L. Georgiou, T. Christodoulou, N. Panayiotou, C. Ioannides, N. Zamboglou and C. Damianou, *J. Appl. Clin. Med. Phys.*, 2022, **23**, e13533.

29 M. Rohrer, H. Bauer, J. Mintorovitch, M. Requardt and H.-J. Weinmann, *Investig. Radiol.*, 2005, **40**, 715–724.
30 É. Tóth, L. Helm and A. E. Merbach, in *Contrast Agents I*, W. Krause, Springer Berlin Heidelberg, Berlin, Heidelberg, 2002, vol. 221, pp. 61–101.
31 C. E. Ribeiro, M. Vinícius-Araújo and A. F. Bakuzis, *ACS Appl. Nano Mater.*, 2025, **8**, 7061–7072.
32 D. Chalise and D. G. Cahill, *Phys. Rev. Appl.*, 2023, **19**, 014055.
33 W. F. Brown, *Phys. Rev.*, 1963, **130**, 1677–1686.
34 S. H. Koenig, R. D. Brown, D. Adams, D. Emerson and C. G. Harrison, *Investig. Radiol.*, 1984, **19**, 76–81.
35 S. H. Koenig and K. E. Kellar, *Magn. Reson. Med.*, 1995, **34**, 227–233.
36 G. Diakova, J. Korb and R. G. Bryant, *Magn. Reson. Med.*, 2012, **68**, 272–277.
37 A. Cárdenas-Blanco, C. Tejos, P. Irarrazaval and I. Cameron, *Concepts Magn. Reson.*, 2008, **32**, 409–416.
38 R. M. Henkelman, *Med. Phys.*, 1985, **12**, 232–233.
39 E. V. Osilla, J. L. Marsidi, K. R. Shumway and S. Sharma, in *StatPearls*, StatPearls Publishing, Treasure Island (FL), 2025.
40 Q. L. Vuong, P. Gillis, A. Roch and Y. Gossuin, *WIREs Nanomed. Nanobiotechnol.*, 2017, **9**, e1468.
41 M. Izydorczyk, S. W. Cui and Q. Wang, in *Food Carbohydrates: Chemistry, Physical Properties, and Applications*, Taylor & Francis, Boca Raton, 2005.
42 A. Roch, R. N. Muller and P. Gillis, *J. Chem. Phys.*, 1999, **110**, 5403–5411.
43 P. Arosio, F. Orsini, F. Brero, M. Mariani, C. Innocenti, C. Sangregorio and A. Lascialfari, *Dalton Trans.*, 2023, **52**, 3551–3562.
44 R. B. Buxton, R. R. Edelman, B. R. Rosen, G. L. Wismer and T. J. Brady, *J. Comput. Assist. Tomogr.*, 1987, **11**, 7–16.
45 R. D. A. Alvares, D. A. Szulc and H.-L. M. Cheng, *Sci. Rep.*, 2017, **7**, 15493.
46 J. Bullivant, S. Zhao, B. Willenberg, B. Kozissnik, C. Batich and J. Dobson, *IJMS*, 2013, **14**, 17501–17510.
47 T. C. Arnold, C. W. Freeman, B. Litt and J. M. Stein, *Magn. Reson. Imaging*, 2023, **57**, 25–44.
48 J. Ren, I. Dimitrov, A. D. Sherry and C. R. Malloy, *J. Lipid Res.*, 2008, **49**, 2055–2062.
49 K. Kuroda, K. Oshio, R. V. Mulkern and F. A. Jolesz, *Magn. Reson. Med.*, 1998, **40**, 505–510.
50 T. Zalewski, M. Kempka, K. Szutkowski, J. Stroud, N. Alghamdi, J. Stoll, Z. Celinski, J. Hankiewicz and S. Jurga, *Presented at Euroismar 2019 Conference*, 2019, 726.
51 A. R. Terry, V. Nogueira, H. Rho, G. Ramakrishnan, J. Li, S. Kang, K. C. Pathmasiri, S. A. Bhat, L. Jiang, S. Kuchay, S. M. Cologna and N. Hay, *Cell Metab.*, 2023, **35**, 2060–2076.
52 R. K. Zwick, C. F. Guerrero-Juarez, V. Horsley and M. V. Plikus, *Cell Metab.*, 2018, **27**, 68–83.
53 S. S. More and X. Zhang, *Investig. Magn. Reson. Imaging*, 2024, **28**, 153.
54 M. Carl, Y. Ma and J. Du, *Magn. Reson. Imaging*, 2018, **50**, 12–16.
55 L. Zhang, X. Zhong, L. Wang, H. Chen, Y. A. Wang, J. Yeh, L. Yang and H. Mao, *Magn. Reson. Imaging*, 2011, **33**, 194–202.
56 W. Liu, H. Dahnke, J. Rahmer, E. K. Jordan and J. A. Frank, *Magn. Reson. Med.*, 2009, **61**, 761–766.